Original Article

Comprehensive Analysis of Heart Rate Variability Using Various Methods

Hadeer Ahmed Mahmoud[1], Yehia S. Mohamed[2]

[1,2]*Electrical Engineering Department, Faculty of Engineering, Minia University, Minia, Egypt.*

[1]*Corresponding Author : hadeer.Ahmed.pg@eng.s-mu.edu.eg*

Abstract - *Over the past two decades, the analysis of Heart Rate Variability (HRV) has garnered considerable traction, serving as a pivotal tool in studying various disease pathologies. HRV analyses encompass methodologies aimed at quantifying Heart Rate (HR) variations non-invasively. This study aimed to conceive, assess, and apply an accessible HRV analysis. The presented analysis integrates four primary categories of HRV techniques. The first two methods are the statistical and time-domain analysis. Moreover, the frequency-domain analysis, nonlinear analysis, and time-frequency analysis have been applied. Assessments of the presented analysis were conducted by conducting HRV analysis on simulated data. The results obtained from simulations indicated the reliability of the proposed analysis as an HRV analysis procedure. The presented analysis stands as a valuable resource, offering researchers an effective tool for conducting HRV analysis.*

Keywords - ECG signals, HRV, IBIs, Time-domain analysis, Frequency-Domain Analysis, Nonlinear analysis, Time-Frequency Domain Analysis.

1. Introduction

Heart Rate Variability (HRV) analysis can be considered a noninvasive approach that assesses fluctuations in the time intervals among successive heartbeats. These variations can reveal an appreciated awareness of the adaptability and responsiveness of the cardiovascular system [1].

By examining HRV, researchers and clinicians gain an understanding of how the heart rate dynamically adjusts in response to various physiological and environmental stimuli. This information is instrumental in gauging the overall health of the cardiovascular system, identifying potential anomalies, and providing indications of the system's regulatory capabilities [2].

Examining Heart Rate Variability (HRV) has evolved into a standard method utilized across a diverse spectrum of clinical and research domains. These encompass a wide array of areas, including the regulation of the Autonomic Nervous System (ANS), risk evaluation for sudden cardiac death, diabetic neuropathy, pharmaceutical assessments, and studies on psychological disorders [3, 4].

HRV, at its core, signifies the alterations in time intervals between successive heartbeats. The analysis of HRV aims to quantitatively measure these variations, which in specific scenarios may serve as indicators of underlying physiological abnormalities. Much like blood pressure and temperature,

Heart Rate (HR) is not a fixed parameter; it dynamically fluctuates inside a range in response to the body's requirements. Well-functioning cardiovascular systems are adept at swiftly recognizing and adapting to the shifting demands placed upon them, facilitating the restoration of balance (homeostasis) and enabling specific activities [2].

Studies on Heart Rate Variability (HRV) detail specific oscillations identified in the Interbeat Interval (IBI) time series linked to autonomic influences on heart rate. Two primary HR oscillations have been defined through computer analysis and pharmacological studies. The High-Frequency (HF) oscillation, typically within the range of 0.150-0.40 Hz [5], is often associated with Respiratory Sinus Arrhythmia (RSA) and can be well-thought-out a measure of pneumogastric activity due to its relation to vague nerve activity. The other primary HR oscillation described in HRV is the Low-Frequency (LF) oscillation, ranging between 0.04 and 0.15 Hz, which encompasses the 10-second rhythm or Mayer wave [6].

While there's some debate on whether the LF oscillation represents solely sympathetic activity, it's generally accepted that LF encompasses a blend of understanding and vagal activity [7]. To validate these HR oscillations, both electrophysiological and pharmacological studies have been conducted on the sympathetic nervous system as well as the parasympathetic nervous system [8]. By selectively blocking

or stimulating sympathetic and vagal activity, researchers were able to establish links between these frequency bands and the branches of ANS.

As atropine, an antagonist for muscarinic acetylcholine receptors, was used in vagal blockades, while beta-adrenergic antagonists like propranolol were employed for sympathetic blockade. These investigations further revealed that vagally mediated changes in heart rate occur more rapidly than sympathetically mediated changes [9].

This discrepancy in response rates is attributed to differences in receptor processes and postsynaptic responses. Studies indicated that muscarinic binding processes primarily occur within the cell membrane. In contrast, adrenergic receptor binding processes involve secondary signaling pathways before membrane ion channel alterations, leading to a longer response time [10].

Apart from LF and HF oscillations, there exist two lesser-described HR oscillations below 0.040 Hertz. The very low-frequency oscillation of VLF; 0.0030-0.050 Hertz, and ultra-low-frequency oscillation of ULF; under 0.0030 Hertz, have received less attention than the preceding bands. VLF may involve thermoregulatory cycles and fluctuations in plasma renin activity [11].

Meanwhile, circadian rhythms are typically the primary contributors to the ULF frequency band [12]. These two oscillations, especially ULF, might be affected by low-frequency trends due to inherent non-stationarities in IBI signals [13]. The description of physiological mechanisms influencing heart rate presented above is not exhaustive. Heart Rate is influenced by multiple feedback and feed-forward systems that interact directly and/or indirectly. The intricate interplay among these systems results in heart rate variations used in HRV analysis [14].

The analysis of the HRV has gained extensive traction among researchers and clinicians, with a continually growing interest in its application. An examination of the National Library of Medicine's Medline database reveals a notable surge in HRV-related publications, with over 1,000 articles in 2009, exceeding 4,000 in the past five years, and a twofold increase in annual HRV publications compared to a decade ago.

This escalating interest has led to the availability of commercial HRV software tailored for clinicians, facilitating cardiovascular disease diagnosis and enabling continuous monitoring. In healthcare, pivotal objectives such as disease classification, treatment strategizing, progress monitoring, and outcome prediction have spurred considerable enthusiasm and exploration of HRV [15]. Despite the widespread utilization of HRV, there remains an ongoing necessity for software packages that encompass updated, validated HRV

analysis methods packaged in an easily accessible platform designed for both researchers and clinicians. The advent of novel techniques and even some current methodologies can yield intricate or unclear results, underscoring the need for interpretive methods that can provide meaningful physiological insights from HRV analyses, especially for clinicians.

Furthermore, standardizing analysis techniques and delineating HRV measures for specific pathophysiological populations, such as heart failure and models inducing heart failure like hyperaldosteronism, represent essential aspects requiring attention in HRV investigation.

The primary objectives of this paper encompass threefold objectives:
(1) To develop a comprehensive HRV analysis aimed at enhancing comprehension of techniques utilized in HRV analysis and
(2) To assess and validate the software using simulated and publicly available data.

2. Obtaining Interbeat Intervals (IBI)

Heart Rate Variability (HRV) analysis employs data series consisting of time intervals derived from ECG signals. These intervals correspond to the time gaps among successive heartbeats, often obtained through detecting R-waves due to their distinctive features in Electro Cardio Grams (ECGs). Typically, the R-wave boasts the highest amplitude among P, Q, S, and T waveforms. Consequently, the interval between consecutive R peaks is identified as the beat-to-beat interval, also referred to as the RR interval. While the R wave is a primary marker for heartbeat identification, other points like the QRS complex are used, leading to the broader term Interbeat Interval (IBI) to describe any beat-to-beat interval. Furthermore, in the context of normal sinus rhythm, RR intervals are represented by NN, which means the term normal-to-normal intervals, representing IBIs excluding ectopic intervals.
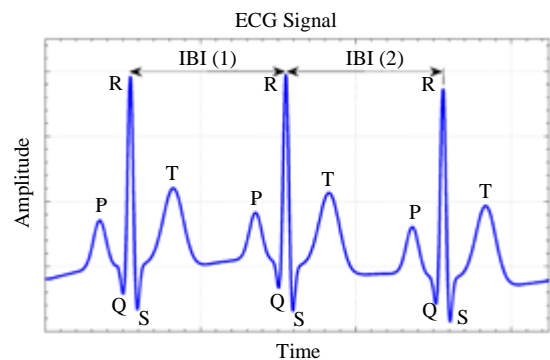

Fig. 1 The process of determining IBI. This simulated ECG comprises three beats, each represented with arbitrary units for time and amplitude. The time intervals associated with the IBI are identified as IBI (1) and IBI (2). Additionally, the ECG morphology is depicted, showcasing five distinct waves: P, Q, R, S, and T.

It's important to note that in scientific literature, terminologies such as IBI, RR, or NN are often used interchangeably to denote the series of intervals, assuming that ectopic beats have been rectified.

Figure 1 illustrates a theoretical ECG and demonstrates the process of determining IBIs using R waves. In this representation, IBI (1), and IBI (2) indicate the initial and subsequent data points within the IBI time series signal. The IBI time series in an ECG segment encompassing N beats can be described as follows:

$$\text{IBI}(n) = \text{beat}(n+1) - \text{beat}(n): 1 \leq n \leq N - 1 \quad (1)$$

This refers to the variable "beat (n)," which denotes the timing or temporal position of the nth beat within the series.

3. Preprocessing
Preprocessing of IBI is frequently necessary before conducting HRV analysis to minimize potential errors. There are three primary types of preprocessing methods applied to IBI data: correction of ectopic beats/intervals, detrending, and IBI resampling.

Previous studies [1, 16] have highlighted HRV analysis errors attributed to ectopic beats and trends within IBIs. In the context of IBI analysis, ectopic beats refer to any intervals that are influenced by abnormal heartbeats. These anomalies can result from false or missed beats, misalignment of fiducial points, or cardiac ectopic activity. Moreover, IBI time series commonly exhibit slowly fluctuating trends that are generally considered inherent in most biological signals, including IBI signals.
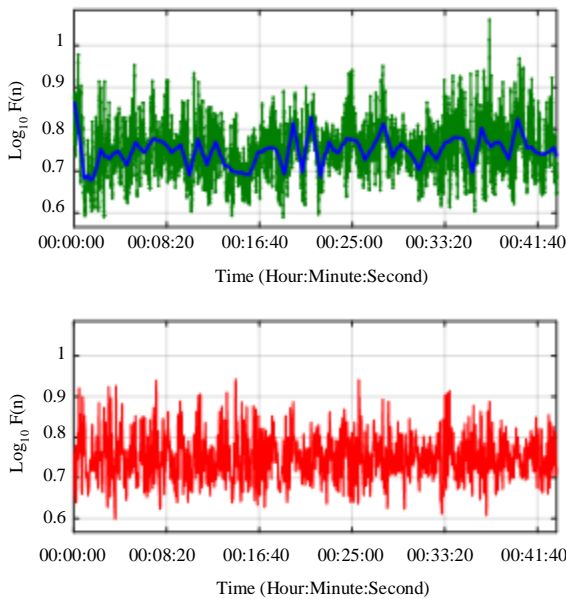

Fig. 2 The IBI signal both before and after the processes of detrending and removal of ectopic intervals, depicting the IBI time series derived from a healthy human

Specific HRV analysis techniques assume that IBI signals are stationary or free of low-frequency trends. For instance, methods utilizing power spectrum estimations based on the Fourier transform require the random variable under examination to be wide-sense stationary (with a mean that doesn't change over time) [1].

To address potential non-stationarities within IBI, detrending is frequently employed prior to conducting HRV analysis [17]. Additionally, these methods assume evenly sampled IBIs, which may not always be the case in IBI signals. Figure 2 depicts an IBI time series before and after the removal of both ectopic intervals and low-frequency trends.

4. Detection of Ectopic Intervals
Before correcting ectopic intervals, it's essential to identify or mark them. Three techniques for ectopic interval detection are discussed here. Although the term "filter" is employed in this context, no alteration to the original IBI takes place during the ectopic interval detection process. The percentage filter identifies intervals that deviate by more than a specified user-predefined percentage, which is commonly around 20.0 percent from the earlier interval [1, 16].

This technique pinpoints sudden or abrupt changes in IBIs. Another approach to detecting ectopic intervals is the standard deviation filter, which identifies outliers by considering intervals lying beyond a user-predefined number of standard deviations from the overall mean IBI, which is usually around 3 SD. Lastly, the median filter entertainments as one of the impulse rejection filters through a set threshold to distinguish ectopic intervals. Moreover, this filter can be expressed as the following:

$$D(n) = \frac{|x(n) - \text{med}(x)|}{1.483 \cdot \text{med}[|x(n) - \text{med}(x)|]},$$
$$\text{if } D(n) \geq \tau, \text{ then not ectopic; else ectopic} \quad (2)$$

Where, x represents a random variable while N denotes its length. Moreover, τ represents the threshold.

4.1. Correction of Ectopic Interval
There are four techniques available to address ectopic intervals identified during the detection process. The first technique involves the straightforward removal of any detected ectopic intervals. Studies have demonstrated that simple ectopic interval removal is just as effective as other replacement methods [18, 19]. Another method involves substituting any ectopic interval with a mean value of w neighboring IBI intervals, which are centered on the ectopic interval, which can be estimated utilizing Equation 3. Similarly, the median method replaces ectopic intervals with a median value of w neighboring IBI intervals centered on the ectopic interval, which can be assessed using Equation 4. Lastly, the cubic spline replacement method replaces ectopic intervals through cubic spline interpolation.

$$ibi'(n) = \text{mean} \left\{ ibi(n + m) : |m| \leq \frac{w-1}{2} \right\} \quad (3)$$

$$ibi'(n) = \text{med} \left\{ ibi(n + m) : |m| \leq \frac{w-1}{2} \right\} \quad (4)$$

5. IBI Detrending

The literature presents various detrending methods aimed at eliminating low-frequency trends. These methods encompass linear and polynomial detrending approaches. Moreover, the wavelet, wavelet packet, and smoothing priors detrending methods can be applied.

5.1. Methods of Linear and Polynomial Detrending

Two straightforward techniques employed for detrending IBI series include linear and polynomial detrending. Linear detrending involves eliminating a linear least-squares-fit from the IBI series. In contrast, polynomial detrending consists of the removal of a second or third-order polynomial fit (in a least squares sense) from the IBI series [20, 21].

5.2. Wavelet Detrending

The process of Wavelet detrending involves decomposing the initial IBI time series into a hierarchy of approximation and detail coefficients through Discrete Wavelet Transform (DWT). Each subdivided sub-band is associated with a specific range of frequencies, where the highest approximation level encompasses the lower frequencies. The elimination of low-frequency trends can be achieved through two methods.

In the initial approach, all wavelet coefficients within the highest level of approximation (representing the lowest frequency) are nullified, followed by executing an inverse DWT. Alternatively, the other technique entails reconstructing solely the uppermost rough calculation sub-band, which is later detracted from the original IBI series [21]. Both approaches effectively apply signal detrending.

5.3. Wavelet Packet Detrending

Wavelet packet detrending is a technique used to remove low-frequency trends from a signal, similar to wavelet detrending. However, wavelet packet decomposition offers a more detailed level of analysis by allowing greater flexibility in choosing decomposition paths and examining various sub-bands. In wavelet packet decomposition, a signal is decomposed into both approximation and detail coefficients, allowing for further division of the signal into sub-bands. This method breaks down the original signal into more detailed components than the regular wavelet transform, offering increased versatility in analyzing and processing the signal.

Wavelet packet detrending operates similarly to wavelet detrending but provides more options for analyzing the signal components by exploring different branches or paths within the decomposition tree. The removal of low-frequency trends in the signal can be achieved by modifying the decomposition coefficients in specific sub-bands or by altering the reconstruction process. This technique offers enhanced control and granularity in dealing with signal trends and features at various frequency levels. Detrending via wavelet packets follows a methodology akin to the detrending process involving DWT detailed earlier.

However, in wavelet packet detrending, the Discrete Wavelet Packet Transform (DWPT) is employed as a replacement for the standard DWT. Here, sub-bands within the wavelet packet structure that harbor frequency components attributed to undesired trends are nullified by setting their wavelet coefficients to zero.

By reconstructing the IBI series through the inverse DWPT, a detrended IBI series is generated [22]. So, similar to the earlier method using DWT, an alternative detrending strategy utilizing DWPT involves decomposing the signal, reconstructing the segments representing unwanted components, and then subtracting these segments from the original signal. This technique offers an effective means to remove specific undesirable trends in the IBI series, providing enhanced control over the detrending process.

5.4. Smoothing Priors

The last detrending technique under consideration has been known as the smoothing priors method [22]. Considering an $N - 1$ long, evenly sampled IBI has been expressed as a composite of stationery component and trend component, denoted as "z = z + z". This approach aims to derive a stationary component considering the signal of the original IBI. The estimated stationary component is formulated as follows:

$$\hat{z}_{\text{stationary}} = z - H\hat{\theta}_\lambda = (I - (I + \lambda^2 D_2^T D_2)^{-1})z \quad (5)$$

In this context, $H \in R^{(N-1)xM}$ signifies the observation coefficient. To simplify, an identity matrix has been employed instead of the observation matrix H. While $\hat{\theta}_\lambda$ stands for the estimation process and calculation of the regression coefficients, where λ denotes the regularization coefficient, while $D_2 \in R^{(N-3)\times(N-1)}$ refers to the second-order difference matrix.

6. IBI Resampling

Furthermost Fourier-based power spectrum guesstimates necessitate signal stationarity and regularity in time sampling. Spectral estimations derived from irregularly sampled signals may present extra harmonics in the power spectrum. Consequently, before conducting specific power spectrum estimations, it's essential to resample the IBI time series. Frequently used resampling methods include cubic spline and linear interpolation.

7. Time Domain HRV Features

7.1. Statistical Measures

The time domain examination of HRV can be commonly divided into statistical and geometric approaches. Statistical time-domain values can be computed directly from the IBI and comprise various metrics:

- Mean IBI: The mean IBI is considered one of the leading indices that can be used for the time domain analysis.
- Standard Deviation (SD) of the NN (SDNN) interval series: SDNN is one of the time domain measures used in HRV analysis. It provides information about the overall variability of the heart rate and reflects both short-term and long-term variations.
- Root Mean Square of Successive Differences (RMSSD) of the IBI series: RMSSD focuses explicitly on the square root of the mean of the sum of the squared differences between adjacent Interbeat Intervals (IBIs) or RR intervals.
- Number of successive differences more significant than a certain threshold in milliseconds (NNx): the NNx metric quantifies the frequency of significant changes in heart rate within a specified time frame, providing insights into the stability and adaptability of the cardiovascular system.
- Percentage of whole intervals differing in excess of a specific threshold in milliseconds (pNNx).

For more extended datasets, two variants of SDNN are used. Both involve segmenting the IBI series into non-overlapping segments, typically five minutes for human IBIs [23]. The first variant, SDNN index or SDNNi calculates the SD of the IBI segment and later determines the mean of all calculated SDs. On the other hand, SDANN calculates the mean IBI of all segments and proceeds the SD of all predetermined values. Mathematically, SDNNi and SDANN can be characterized as follows:

$$\text{SDNNi} = \frac{1}{M} \sum_{i=1}^{M} \text{SDNN(i)} \qquad (6)$$

$$\text{SDANN} = \sqrt{\frac{1}{M-1} \sum_{i=1}^{M} \left[\text{meanIBI (i)} - \overline{\text{meanIBI}} \right]^2} \quad (7)$$

SDNN(i) refers to the SDNN value of the $i - \text{th}$ IBI segment, where mean IBI (i) signifies the mean IBI of the $i - \text{th}$ IBI segment, and M stands for the total number of segments considered. Certainly, RMSSD, an additional HRV metric, encapsulates temporal information by quantifying the root of the mean-squared difference among the successive RR intervals. This metric primarily replicates the short-term variability within the heart rate and can be calculated as the following:

$$\text{RMSSD} = \sqrt{\frac{1}{N-1} \sum_{i=1}^{N-1} (\text{RR}_i - \text{RR}_{i-1})^2} \qquad (8)$$

RR_i represents the ith RR interval, while N denotes the entire number of RR intervals. The RMSSD provides insights into short-term fluctuations in heart rate, offering valuable information about the parasympathetic nervous system's influence on heart rate regulation. Additionally, the ratio between SDNN and RMSSD is another metric used to assess the balance between the long and the short-term variability in heart rate.

7.2. Geometric Measures

Geometric HRV measures involve calculations derived from geometric patterns based on the IBI series [23, 24]. The histogram of IBI is one commonly utilized geometric pattern. From the IBI histogram, two indices are often derived. The first index is the HRV triangular (HRVti). The second one is the Triangular Interpolation of the NN Interval Histogram (TINN). Figure 3 depicts the histogram of a hypothetical series of IBI, with D(t) representing the density distribution.

The highest value of D(t) is symbolized as Y and is positioned at t = X. HRVti can be calculated with the division of the integral area under the D(t) by the extreme of Y. If the distribution D(t) is on a discrete horizontal scale, the area integral corresponds to the total number of IBI intervals, designated as N IBI. Moreover, in this representation, D(t) signifies the distribution of samples; meanwhile, q(t) denotes a triangular function tailored to align with D(t) with the minimization of the integral of the squared division among D(t) and q(t). Here, Y denotes D(X), which is equivalent to the maximum value of D in the series. Therefore, HRVti can be obtained by:

$$\text{HRVti} = \frac{N_{\text{IBI}}}{Y}. \qquad (9)$$

To calculate TINN, values N and M are set along the time axis, while a triangular function q(t) can be established as the following mathematical representation of that $q(t) = 0$ for $M \leq t \leq N$. The peak of this triangle occurs at $q(X) = Y$. Determination of the triangle base, defined by M and N, involves minimizing the integral of the expression $\int_0^{+\infty} (D(t) - q(t))^2 dt$ dt over the range 2 to 0. Ultimately, TINN is expressed in milliseconds and computed as per the methodology detailed in [1, 23].

$$\text{TINN} = M - N.$$

The results of the time domain analysis have been recorded in Table 1. The table lists various time domain indices such as maximam, minimam, mean, and median indices. Moreover, the SDNN, SDANN, NNx, pNNx, RMSSD, SDNNi, mean HR, and sdHR can be calculated. In addition, HRVTi, and TINN have been computed. The results of the IBI histogram and HRV histogram have been shown in Figure 4.

Table 1. Time domain analysis results

Indices	Unit	Value
Max	(ms)	1061
Min	(ms)	590
Mean	(ms)	747.6
Median	(ms)	746
Sdnn	(ms)	65.9
Sdann	(ms)	58.4
Nnx	(count)	362
Pnnx	(%)	10.4
Rmssd	(ms)	33.5
Sdnni	(ms)	115.4
Meanhr	(bpm)	80.9
Sdhr	(bpm)	7.1
Hrvti	(ms)	11.2
Tinn	(ms)	294.4
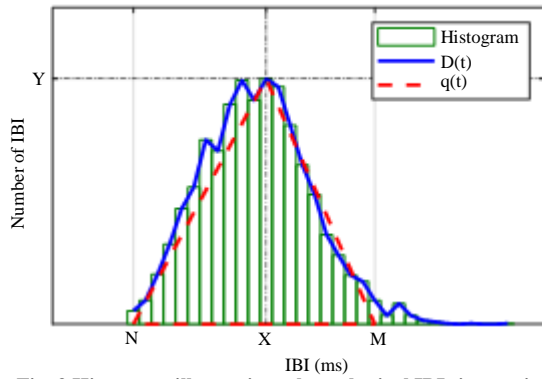
Fig. 3 Histogram illustrating a hypothetical IBI time series

Fig. 4 IBI histogram and HRV histogram

8. Frequency-Domain Analysis

Fluctuations in HR are commonly acknowledged for their periodic nature, spanning various time scales. To quantify these fluctuations within the IBI, the PSD can be calculated. This PSD reveals the spectral power density of a time series concerning frequency, providing insights into the contribution of different frequencies to the overall signal. In the context of frequency-domain HRV analysis, attention is focused on four primary frequency bands: ULF, VLF, LF, and HF. For humans, these bands are typically defined as $0.0 - 0.00330$ Hertz for ULF, $0.0030 - 0.040$ Hertz for VLF, $0.040 - 0.150$ Hertz for LF, and $0.150 - 0.40$ Hertz for HF, correspondingly. Various methods exist for estimating the PSD, among which Fast-Fourier Transform (FFT) as well as Autoregressive (AR) modelling might be widespread in HRV spectral analysis. Methods like Bartlett (1948), Blackman and Tukey (1958), and Welch (1967) can be FFT-based classical power spectrum estimates considered non-parametric as they do not assume how the data are generated. On the other hand, AR power spectrum methods are parametric as they operate based on certain assumptions.
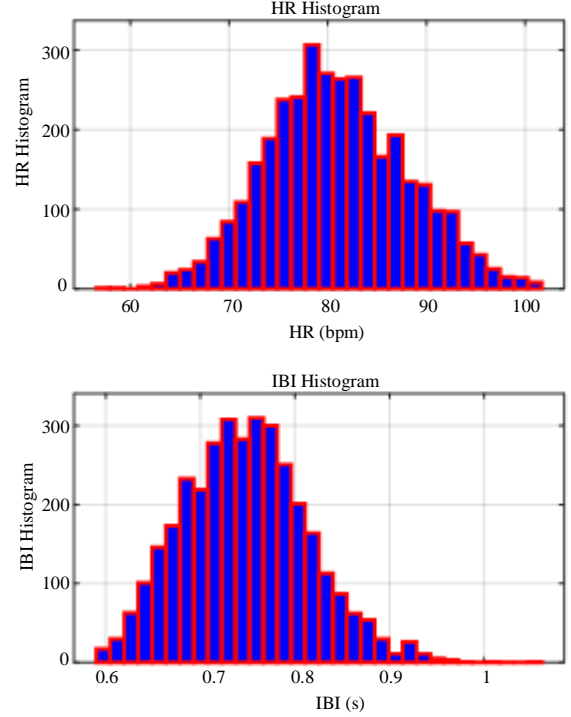
However, both FFT and AR-based PSD estimates necessitate stationary signals as well as evenly sampled time signals, which aren't inherent characteristics of IBI signals. Consequently, alternatives such as Lomb-Scargle periodogram and wavelet transform-based methods are gaining popularity due to their divergence from these stringent requirements. Lomb-Scargle does not mandate resampling, while wavelet transform-based estimates don't rely on signal stationarity. Notably, FFT and AR-based PSD guesstimates, despite their extensive use in HRV analysis, encounter limitations in biological signals such as IBI series.

8.1. Welch Periodogram

To comprehend Welch's periodogram, it's essential to grasp the concepts of the Discrete Fourier Transform (DFT), the fundamental periodogram, as well as the altered periodogram. The $N - $ point DFT of a stochastic variable $X(n)$ is expressed as follows:

$$DFT_x(f) = \sum_{n=0}^{N-1} X(n)e^{-i2\pi fn}$$

In practical applications, the Fast Fourier Transform (FFT) can be considered the employed general method for rapid computations of the DFT due to its efficiency. The periodogram, an extension of the Discrete Fourier Transform (DFT), serves as a fundamental technique for estimating the PSD, and it can be expressed as:

$$P(f) = \frac{1}{N}\left|\sum_{n=0}^{N-1} X(n)e^{-i2\pi fk/L}\right|^2 k = 0,1,\dots,L-1 \quad (10)$$

To minimize spectral leakage in the periodogram, one approach involves integrating a weighted windowing function, such as Hamming or Hanning, into the input series. This technique assigns less weight to the data at the edges of the time series compared to the data closer to the center. As a result, the modified periodogram can be expressed as:

$$P_M(f) = \frac{1}{MU}\left|\sum_{n=0}^{M-1} X(n)w(n)e^{-i2\pi fn}\right|^2$$
$$i = 0,1,\dots,L-1 \tag{11}$$

Where, $U = 1/M\sum_{n=0}^{M-1} w^2(n)$, Ultimately, to minimize the variance in periodogram estimation, the Welch technique divides the data series over N overlapping segments. Similar to the adapted periodogram, the Welch approach incorporates a weighting window toward mitigating spectral leakage; however, this weighting has been applied to all segments individually. Subsequently, an averaged PSD can be computed utilizing all segments. The PSD estimated by the Welch periodogram can be expressed as:

$$P_W(f) = \frac{1}{N}\sum_{i=0}^{N-1} P_{M,i}(f) \tag{12}$$

Here, $P_{M,i}(f)$ represents the ith adapted periodogram derived.

8.2. Burg Periodogram
Autoregressive spectral estimation methods deviate from non-parametric approaches by aiming to create a model of the data rather than directly estimating the Power Spectral Density (PSD). Various modeling techniques are available for Auto Regressive (AR) spectrum estimation, with the Burg method being the most prevalent [17, 25]. The power spectrum of a pth order autoregressive process can be expressed as follows:

$$P_{Burg}(f) = \frac{1}{f_s}\frac{\varepsilon_p}{\left|1+\sum_{k=1}^{p} a_p(k)e^{-2\pi jkf/f_s}\right|^2} \tag{13}$$

Here, ε_p represents the overall least square error, f_s denotes the sample rate and a_p stands for the parameters of the Burg AR model. According to Boardman et al., opting for a model order ranging between $p = 16 - 20$ can be considered suitable for the HRV analysis using human IBI resampled at 2-4 Hz.

8.3. Lomb-Scargle Periodogram
The Lomb-Scargle Periodogram (LSP) is an approach for estimating PSD that doesn't necessitate resampling; it exclusively uses existing data. Essentially, the LSP assesses the frequency spectrum by fitting sinusoids to the data using a least squares approach. In contrast to Welch's periodogram, LSP doesn't involve the application of weighted windowing functions to the data due to the difficulty of applying standard weighting techniques to unevenly sampled data.

The LSP for a real-valued, non-uniformly sampled data sequence X with a length of N for arbitrary times tn can be calculated as the following:

$$P_{LS}(f) \equiv \frac{1}{2\sigma^2}\left\{\begin{array}{l}\frac{\left[\sum_{n=1}^{N}(X(t_n)-\overline{X})\cos(2\pi f(t_n-\tau))\right]^2}{\sum_{n=1}^{N}\cos^2(2\pi f(t_n-\tau))}\\ + \frac{\left[\sum_{n=1}^{N}(X(t_n)-\overline{X})\sin(2\pi f(t_n-\tau))\right]^2}{\sum_{n=1}^{N}\sin^2(2\pi f(t_n-\tau))}\end{array}\right\} \tag{14}$$

In this equation, $\overline{X}$ represents the mean of the time series while σ^2 denotes its variance.

$$\tau \equiv \tan^{-1}\left(\frac{\left(\sum_{n=1}^{N}\sin(4\pi ft_n)\right)}{\left(\sum_{n=1}^{N}\cos(4\pi ft_n)\right)}\right) \tag{15}$$

τ represents a frequency-dependent time delay, specifically demarcated to render the periodogram less sensitive to time shifts. For a more comprehensive understanding of the Lomb-Scargle Periodogram (LSP), further details can be found in [1].

Research conducted by Clifford et al. demonstrated that removing up to 20% of the data points due to ectopic beats in an IBI signal did not introduce a 'significant' error in frequency-domain HRV measures using LSP [1, 25]. Due to its resilience against errors resulting from data removal and resampling, LSP may emerge as the preferred method for estim ating power spectra in HRV.
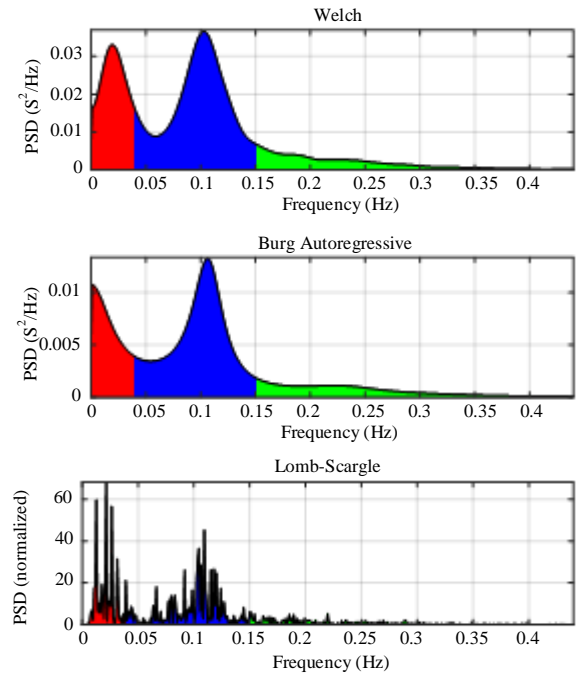

Fig. 5 A comparative view of PSD estimates, encompassing (a) The Welch periodogram, (b) The Burg autoregressive periodogram, and (c) The LSP estimates.

An evaluation of the Welch, Burg, as well as Lomb-Scargle (LS) periodograms, is depicted in Figure 5. The HRV frequency bands can be categorized as very low frequency (VLF, $0.0 - 0.040$ Hertz), low frequency (LF, $0.040 - 0.150$ Hertz), as well as high frequency (HF, $0.150 - 0.40$ Hertz). These PSDs are calculated using reprocessed IBI data obtained from healthy individuals. The power values are depicted as a percentage of the total power. For more demonstration, the results of the frequency analysis domain have been listed in Table 2.

Table 2. Frequency domain analysis using Welch

HRV Variable	Subject and Unit	Welch	LS	Burg
aVLF	(ms_2)	987.36	0.006	274.06
aLF	(ms_2)	2037.93	0.01	659.33
aHF	(ms_2)	484.09	0.003	161.01
aTotal	(ms_2)	3509.38	0.019	1094.39
pVLF	(%)	28.1	33	25
pLF	(%)	58.1	53	60.2
pHF	(%)	13.8	14	14.7
nLF	(%)	0.808	0.791	0.804
nHF	(%)	0.192	0.209	0.196
LFHF		4.21	3.774	4.095
peakVLF	(Hz)	0.02	0.02	0
peakLF	(Hz)	0.1	0.11	0.11
peakHF	(Hz)	0.22	0.22	0.22

9. Time-Frequency Analysis

HRV examination based on frequency-domain approaches solely provides insights into the distribution of power in the frequency domain of the IBI signal. Nevertheless, it doesn't offer info concerning how the spectrum evolves. Approaches enabling the simultaneous examination of mutual time and frequency evidence can be commonly labeled as Time-Frequency Domain Analyses (TFDA). Similar to the FDA, the TFDA calculates measures related to VLF, LF, as well as HF.

The prime methods used for TFDA include the windowed Fourier transform (known as the Short-Time Fourier Transform, STFT) and the Continuous Wavelet Transform (CWT) [1]. To encompass spectral estimation methods beyond the fourier change, the term "windowed periodogram" can be applied instead of the windowed Fourier transform. This broader term allows for the inclusion of methods like the windowed Burg periodogram as well as windowed LSP.

9.1. Windowed Periodogram

The windowed power spectrum extends the fundamental PSD concept by segmenting the data into consecutive (either overlapping or non-overlapping) windows. Each segment's PSD is then calculated individually, akin to Bartlett's and Welch's methods. However, these techniques lose temporal information by averaging all PSDs into a single one. In contrast to Welch's approach, the windowed periodogram allows for the application of other PSD computation methods, such as the Burg periodogram.

Plotting PSD values on a two-dimensional plane with frequency and time as the vertical and horizontal axes, respectively, results in a spectrogram, as depicted in Figure 5. Two alternative methods that have been applied are the windowed Burg periodogram and the windowed LSP. For the windowed Burg periodogram, the entire data series undergoes resampling before being divided into segments of equal length.

Subsequently, the PSD for each segment is computed using the Burg periodogram. Similarly, the windowed LSP follows a comparable process. Initially, the data is segmented into equal time-length segments. Due to the uneven sampling of IBIs, each segment might contain a different data length. Finally, the LSP for each segment is computed.

9.2. Wavelet Transforms

Wavelet transforms, a relatively recent but highly favored tool, have gained immense popularity for analyzing and compressing various types of time signals. The term "wavelet" denotes a compact waveform of finite length and energy. Similar to the Fourier transform, the wavelet transform dissects a signal into its fundamental constituents. However, dissimilar to the Fourier transform, wavelet transforms are capable of handling non-stationary signals and are not restricted to a singular set of basis waveforms for signal dissection.

While Fourier transforms rely on sinusoidal waveforms, wavelet transforms encompass an infinite set of basis waveforms or mother wavelets, provided they adhere to specific mathematical criteria. This property potentially unveils information that might remain obscured by methods like Fourier analysis. Acharya et al. emphasize that "bio-signals often display self-similarity patterns in their distribution, and a wavelet, akin to its fractal shape, would yield superior results in terms of pattern clarity and distinction."

A condensed explanation based on Acharya's understanding of wavelet transform concepts is as follows: the wavelet transform involves correlating a mother wavelet with sections of the original signal, resulting in wavelet coefficients. By shifting or translating the mother wavelet across the time signal, a set of coefficients is generated along the time axis. Then, the mother wavelet undergoes contraction or dilation, producing coefficients across the time series at various time scales. Here, the term "scale" is akin to frequency, or more precisely, the pseudo frequency (average frequency).

The scaled wavelets are normalized, ensuring that each carries an identical energy load. The scale can be envisioned as the width of the wavelet, while the translation denotes its temporal position. Larger scale values correspond to smaller wavelet sizes and, therefore, higher frequencies. This study focuses on three types of wavelet transforms the CWT, the DWT, and the DWPT-the primary distinctions among the three lies in how the wavelet function is scaled and decoded.

9.3. Continuous Wavelet Transform

For a specific signal $x(t)$ and a wavelet function, denoted as $\psi_{a,b}(t)$, the Continuous Wavelet Transform (CWT) coefficients can be expressed as follows:

$$W(\tau, \alpha) = \frac{1}{\sqrt{\alpha}} \int_{-\infty}^{\infty} x(t)\psi^* \left(\frac{t-\tau}{\alpha}\right) dt \qquad (16)$$

The formula depicts the complex conjugate of the mother wavelet $\psi(t)$, denoted as $\psi^*(t)$, along with the dilation parameter α and the location parameter τ. The bivariate function $W(\tau, \alpha)$ represents how closely $x(t)$ resembles a wavelet scaled by α at a specific time τ. In theory, the CWT wavelet coefficients are computed for extremely minute translations and scaling factors.

Nonetheless, in practical applications of the CWT, achieving a balance between the quantity of translations and scales is crucial to maintaining reasonable computational efficiency. Many software implementations of the CWT permit users to define the number of scales for computation.

When the CWT coefficients are visualized on a two-dimensional plane, with scale and location representing the vertical and horizontal axes, respectively, it generates a scalogram, as depicted in Figure 6. The frequency axis, defined using a logarithmic scale, showcases the equivalent frequency of the CWT scales.

9.4. Discrete Wavelet Transform

In the scenario of DWT and DWPT, the process of scaling and translations occurs more discretely compared to CWT. In DWT, scaling and translations are based on powers of 2 or dyadic blocks, such as 2^1, 2^2, and so on. The dilation function can be typically characterized as a tree structure composed of low and high-pass filters. The initial stage of this tree divides the original signal into two components: detail (high frequency) and approximation (low frequency).

Figure 6 illustrates the detail and approximation components for three levels of decomposition, denoted as A and D. In DWT, only the approximation components undergo further decomposition into finer components. Conversely, in DWPT, both branches of the tree are divided into finer components.

Figure 7 depicts the tree structure for DWPT over three levels of decomposition. The horizontal axis represents the frequency range as a fraction of the Nyquist frequency. DWPT can extract all frequency bands with equal resolution. The diagram has been adapted from Tanaka and Hargens.
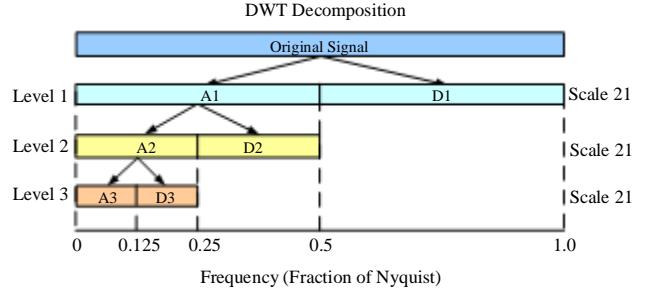

Fig. 6 Decomposition trees: These diagrams display the breakdown of an initial signal into three levels using DWT
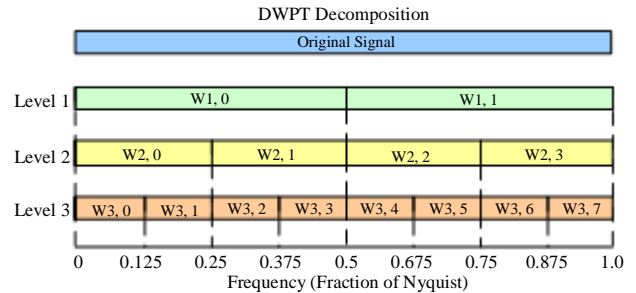

Fig. 7 Decomposition trees: These diagrams display the breakdown of an initial signal into three levels using DWPT

The process of quantifying HRV measures from time-frequency analysis via Continuous Wavelet Transform (CWT) follows a method comparable to that employed for the windowed periodogram. Both approaches have the flexibility to utilize either the instantaneous or global power spectrums.

To derive HRV measures using instantaneous power methods, the square of the wavelet coefficients is integrated across the desired frequency band f1 to f2. Transforming wavelet scales into frequencies is necessary for integrating across a frequency band. The interpretation of the time-scale map (scalogram) should be adapted into a time-frequency map (spectrogram). The instantaneous power within the frequency band f1 to f2 is mathematically expressed as:

$$P_{CWT}(t) = \frac{1}{C_\psi} \int_{\alpha_1}^{\alpha_2} |W(t, \alpha)|^2 \frac{d\alpha}{\alpha^2} = \frac{1}{C_\psi f_\psi} \int_{f_1}^{f_2} \left|W(t, f_\psi/f)\right|^2 df. \quad (17)$$

The wavelet counterpart to an averaged periodogram has been known as the global wavelet spectrum, and it can be defined as follows:

$$\overline{W}^2(t) = \frac{1}{N} \sum_{n=0}^{N-1} |W_n(t)|^2 \qquad (18)$$

9.5. Results of Time-Frequency Analysis

Case 1: Spectrogram utilizing the windowed Burg periodogram.

Figure 8 exhibits the spectrogram, surface, LF/HF ratio, and LF/HF power acquired through windowed periodograms, utilizing preprocessed IBI data from a healthy human employing the windowed Burg periodogram. The quantification of HRV via TFDA employing windowed periodograms can be accomplished using the Burg periodogram. Initially, this method involves computing an averaged or overall power spectrum, followed by the derivation of representative frequency-domain HRV metrics like $LF, HF,$ and LFHF. Although averaging the power spectrum sacrifices time resolution, it effectively minimizes variances by amalgamating numerous power spectra.

However, this approach may somewhat compromise the objective of time-frequency analysis. An alternative method entails computing HRV metrics for each segment, subsequently deriving an average HRV measure. This secondary approach yields discrete instantaneous frequency-domain measures that fluctuate over time, such as LF(t) as well as LFHF(t). By utilizing the LFHF instantaneous time series, an additional index known as the ratio of LFHF ratios (rLFHF) can be extracted]. This metric serves as an indicator of the "global" sympathetic-parasympathetic equilibrium. Consider envisioning a line drawn at LFHF = 1.0 on the instantaneous LFHF plot. Over the threshold of LFHF > 1.0 suggests sympathetic dominance, while under LFHF < 1.0 implies parasympathetic dominance. The rLFHF ratio can be computed by determining the ratio of the confined area over the LFHF = 1.0 line w.r.t the enclosed area under it.
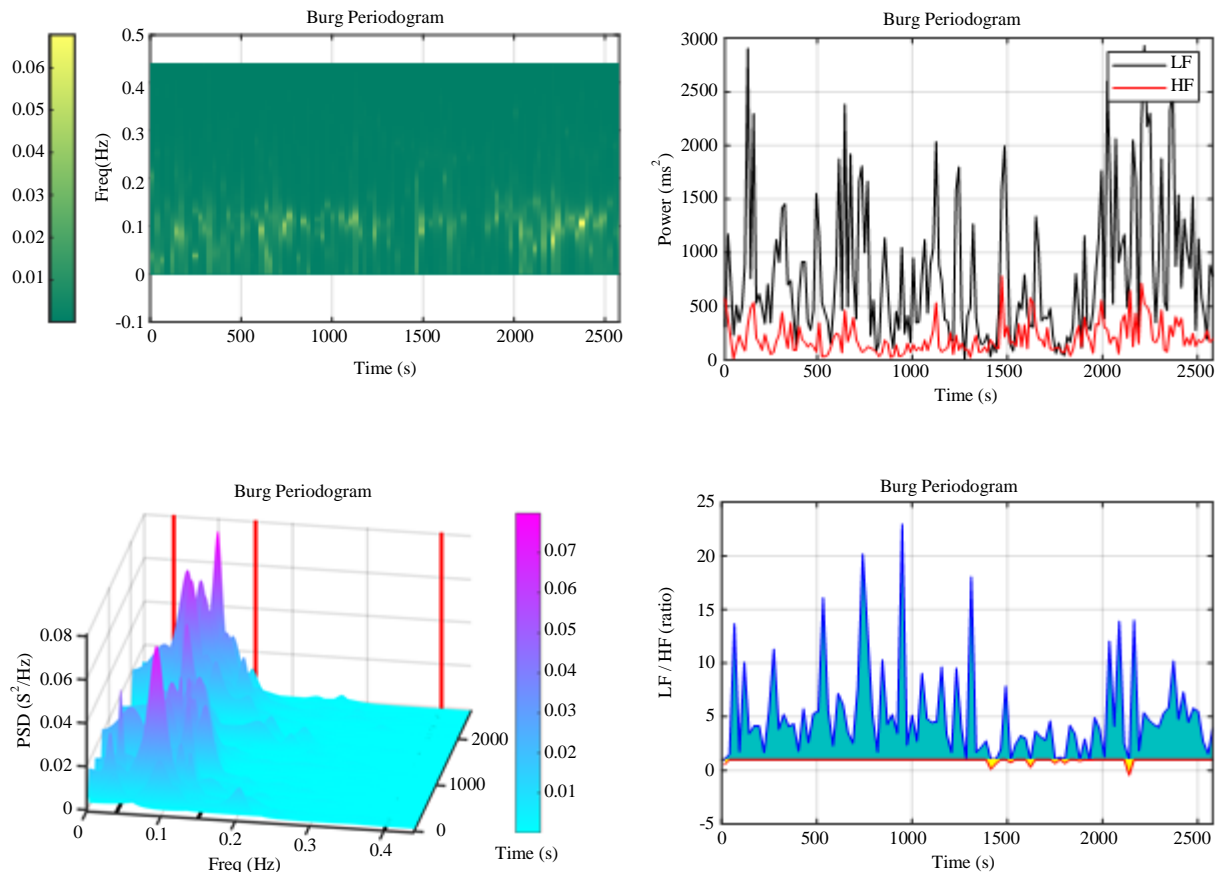

Fig. 8 The spectrogram, surface, LF/HF ratio, and LF/HF power obtained utilizing the windowed Burg periodogram

Case 2: Spectrogram employing the windowed Lomb-Scargle periodogram

Figure 9 displays the spectrogram, surface, LF/HF ratio, and LF/HF power obtained via windowed periodograms, utilizing preprocessed IBI data from a healthy human through the windowed Lomb-Scargle Periodogram. The quantification of HRV through time-frequency analysis using windowed

periodograms can be accomplished by employing the LSP periodogram. Initially, this methodology involves computing an averaged or comprehensive power spectrum, followed by deriving typical frequency-domain HRV metrics such as LF, HF, and LFHF. While averaging the power spectrum diminishes time resolution, it effectively reduces variances by amalgamating numerous power spectra. However, this strategy may somewhat compromise the goal of time-

frequency analysis. An alternative approach involves computing HRV metrics for each segment, subsequently deriving an average HRV measure. This secondary method generates discrete instantaneous frequency-domain measures that fluctuate over time, including LF(t), and LFHF(t).

Utilizing the LFHF instantaneous time series allows the extraction of an additional index known as the ratio of LFHF ratios (rLFHF). This metric serves as an indicator of the "global" sympathetic-parasympathetic equilibrium.
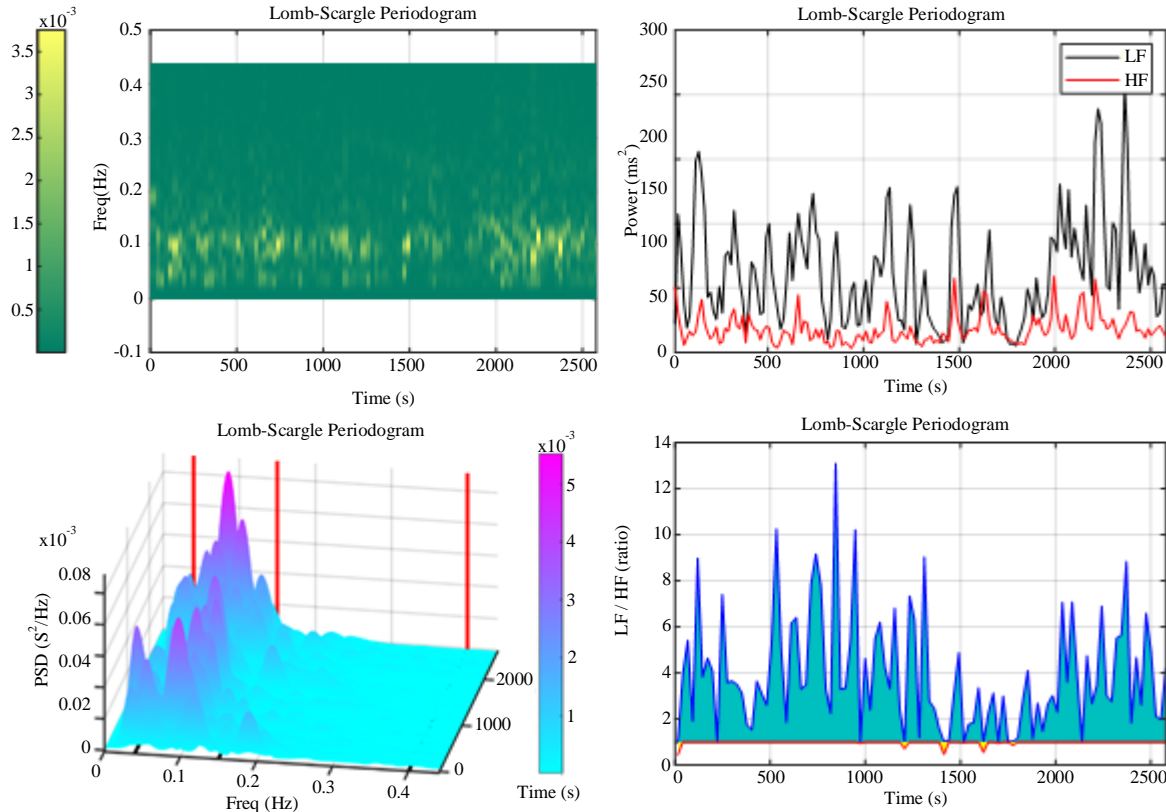

Fig. 9 Spectrogram, surface, LF/HF ratio, and LF/HF power obtained employing the windowed LSP

Case 3: Wavelet transforms

Figure 10 showcases the spectrogram, surface, LF/HF ratio, and LF/HF power derived from windowed periodograms utilizing preprocessed IBI data from a healthy individual and employing the wavelet transforms. Evaluating HRV through time-frequency analysis using windowed periodograms can be accomplished using wavelet changes. Initially, this approach entails computing an averaged or aggregate power spectrum, leading to the derivation of typical frequency-domain HRV metrics like LF, HF, and LFHF. While this method of power spectrum averaging compromises time resolution, it effectively minimizes variances by combining multiple power spectra. However, this amalgamation might somewhat hinder the primary objective of time-frequency analysis. An alternative methodology involves computing HRV metrics for individual segments, subsequently culminating in an average HRV measure. This secondary approach yields discrete instantaneous frequency-domain measures that exhibit temporal fluctuations, encompassing LF(t) and LFHF(t).

Table 3. Time-frequency analysis using Time-Freq: AR

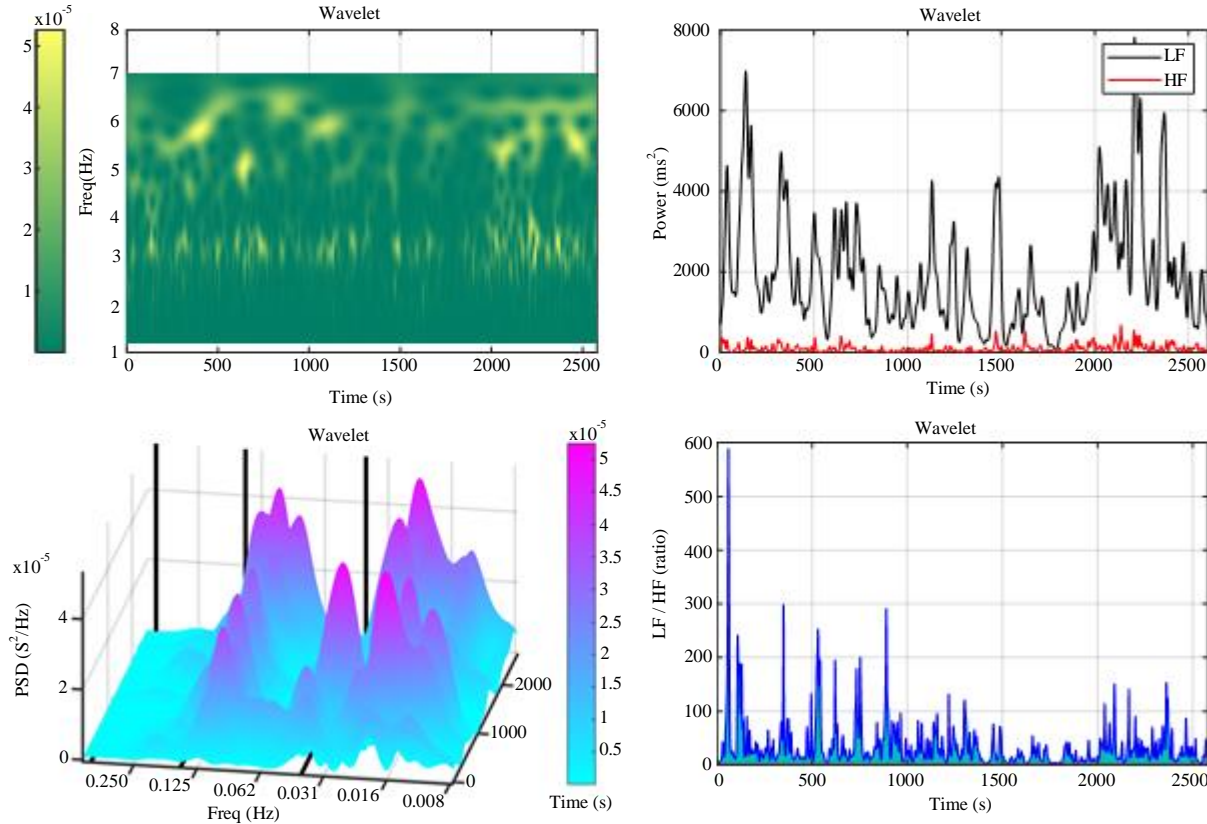| HRV Variable	Subject	Wavelet	LS	Burg
aVLF	(ms_2)	965.23	6.28	168.87
aLF	(ms^2)	1987.39	60.63	802.53
aHF	(ms^2)	557.31	18.05	203.43
aTotal	(ms^2)	3509.93	84.96	1174.83
pVLF	(%)	27.5	7.4	14.4
pLF	(%)	56.6	71.4	68.3
pHF	(%)	15.9	21.2	17.3
nLF	(%)	0.781	0.771	0.798
nHF	(%)	0.219	0.229	0.202
LFHF		3.566	3.36	3.945
peakVLF	(Hz)	0.01	0.04	0
peakLF	(Hz)	0.1	0.1	0.1
peakHF	(Hz)	0.15	0.34	0.24
rLFHF		65535	13	11.28571

Fig. 10 Spectrogram, surface, LF/HF ratio, and LF/HF power obtained employing the windowed Wavelet transforms

Utilizing the LFHF instantaneous time series enables the derivation of an additional index termed the ratio of LFHF ratios (rLFHF). The main results of the time-frequency analysis have been recorded in Table 3 using the three approaches of HRV analysis.

10. Nonlinear Analysis

Given the possibility that heart rate control might include nonlinear elements, there's a growing curiosity in exploring HRV through approaches beyond traditional linear methods like time-domain and spectral analysis. These alternative methodologies fall under the category termed nonlinear HRV analysis. Studies have indicated that the reduction in complexity of IBI signals and the absence of fractal-like scaling patterns could be common traits in cardiac disorders. Techniques such as Poincaré plot analysis, entropy-based metrics, and fractal-based measures are a subset of the various HRV analysis methods employed in this domain.

10.1. Poincaré Plot

The Poincaré plot, also known as the first-return map and named after Henry Poincaré, graphically represents IBI intervals against their preceding IBI interval. This visualization technique is a form of nonlinear analysis utilized to measure self-similarity. HRV metrics derived from Poincaré plots are built on the premise that each IBI is influenced by its preceding one [22]. Successive IBI pairs

form an attractor in the Poincaré plot. Usually, an ellipse is fitted to the plotted data, with its long axis aligned along the line of identity defined by y = x. In Figure 8, you can see an illustration of a Poincaré plot generated from IBI data of a healthy individual. When the center or attractor of the ellipse aligns with the mean IBI ($\overline{IBI}$), the line perpendicular to the line of identity and passing through the mean is defined by:

$$y = -x + 2\overline{IBI} \qquad (19)$$

Data points above the line of identity signify a longer IBI compared to the previous one, while points below it indicate a shorter IBI. Standard Deviations along the line of identity (SD2) and perpendicular to it (SD1) respectively signify the magnitude of the major and minor axes of the ellipse. SD1 represents the variability from beat to beat or short-term variability, while SD2 represents the continuous or long-term variability.

It's essential to note that while the ellipse aids in visualizing the data, the numerical values of SD1 and SD2 hold the crucial information. Additionally, the ratio of SD1 to SD2 has been suggested as strongly correlated with mortality in adults with postoperative ischemia. Figure 11 shows the Poincaré Plot illustrating healthy human IBI data. Moreover, the results and indices have been recorded in Table 4.
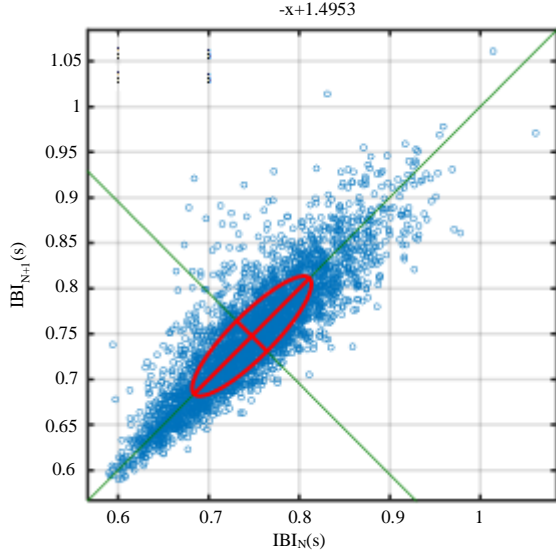
Fig. 11 Poincare plot illustrating healthy human IBI data

Table 4. Poincare indices illustrating healthy human IBI data

HRV Variable	SD1	SD2
Subject	(ms)	(ms)
Sample Data	23.7	90.1

10.2. Detrended Fluctuation Analysis

Fractal scaling and self-similarity are concepts that revolve around the notion of breaking down a system or structure into smaller parts, each resembling the whole but on varying scales. The Sierpinski triangle stands as a classic example of fractal geometry.

In nature, fractals manifest in phenomena like snowflakes, coastlines, crystals, and certain types of ferns. In the context of IBI analysis, the scale pertains to time. Detrended Fluctuation Analysis (DFA) seeks to assess the fractal-like or self-similar characteristics within non-stationary time series. It is an adapted form of root-mean-square analysis applied to non-stationary signals.

It measures the root-mean-square fluctuation of an integrated and detrended time series across different scales. The obtained values are subsequently plotted against the scale size on a log-log plot, as illustrated in Figure 12. Let's consider an IBI time series with a length of N. This series undergoes integration using a summation process, followed by detrending to remove the trend or the baseline from the integrated series.

This detrended series is then divided into smaller segments of varying lengths or scales. The root-mean-square fluctuation is computed for each segment across different scale sizes. These values are plotted on a logarithmic scale against the corresponding scale sizes on another logarithmic scale, as shown in Figure 12.

This log-log plot allows the assessment of the relationship between the fluctuation and scale size, revealing the existence of fractal-like patterns within the time series.

$$y(k) = \sum_{i=1}^{k} [IBI(i) - \overline{IBI}] \tag{20}$$

Where,
y(k) represents the kth value within the integrated series,
IBI(i) signifies the ith interbeat interval, and

$\overline{IBI}$ stands for the average interbeat interval across the entire time series.

The integrated time series is then partitioned into segments of length n. In each segment, a most minor square line is fitted to the data to delineate the local trend, denoted by $y_n(k)$. Subsequently, the integrated time series undergoes detrending by subtracting this local trend, $y_n(k)$, from each respective segment. Finally, the root-mean-squared fluctuation of the integrated and detrended time series is computed by:

$$F(n) = \sqrt{\frac{1}{N} (\sum_{k=1}^{N} [y(k) - y_n(k)]^2)} \tag{21}$$

The variable n signifies the window or scale size, and F(n) is computed across a user-defined range of time scales. The logarithmic relationship between log(F) and log(n) serves to determine the scaling exponent, denoted as α, of the interbeat interval time series. Typically, two distinct linear segments appear on the log-log plot, characterizing the short-term scaling, α_1, and the long-term scaling, α_2.

A breakpoint distinguishes these segments, characteristically found around 12-16 beats. Illustrated in Figure 12 is the DFA plot for a typical human IBI signal, depicting a breakpoint at 12 beats. The results of such case analysis are listed in Table 5.
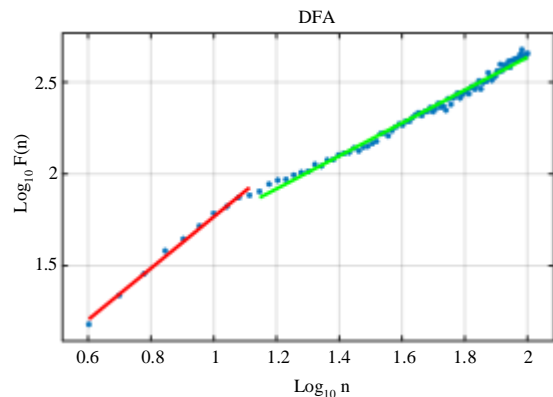

Fig. 12 Shows the detrended fluctuation analysis applied to healthy human data, showcasing the short-term scaling exponent (α1) and long-term scaling exponents (α2). The breakpoint appears at the 12-beat mark.

Table 5. Detrended fluctuation analysis applied to healthy human data

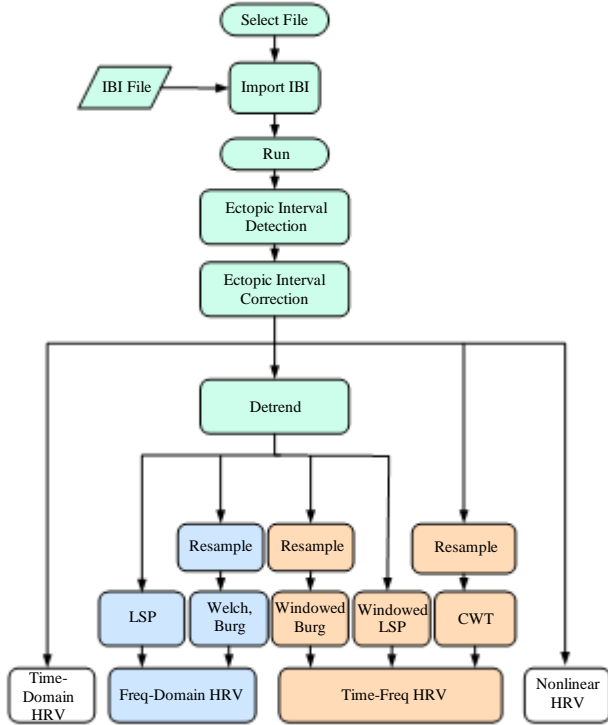| HRV Variable	Sample	αAll	α1	α2
Value	1.782	0.924	1.4	0.896

Fig. 13 Sequence involved in heart rate variability analysis

11. Discussion

The validation of the presented analysis methods has been shown through the study and analysis of a data set of IBI. This section encompasses the validation assessments designed to verify the analysis outcomes derived from the presented methods for HRV. The initial evaluation involved the computation of time-domain, frequency-domain, and time-frequency HRV measures using computer-simulated ECG signals. Figure 13 illustrates the sequence involved in heart rate variability analysis to calculate HRV metrics. The preprocessing steps encompass ectopic interval identification, replacing ectopic intervals, and detrending the Interbeat Intervals (IBI). Earlier sections have elaborated on the specifics of HRV analysis.

12. Conclusion

HRV assessment can be conducted precisely through the utilization of the time domain, frequency domain, and nonlinear methods, ensuring consistent replicability. The intricate neural network connections that regulate heart rate enable the exploration of how various internal and external factors impact it. However, the complexity inherent in these connections presents a challenge for analysis, demanding controlled environments to eliminate unwanted influences.

This criterion is scarcely met in clinical practice. It is imperative to establish rigorously standardized HRV tests that encompass diverse conditions such as breathing patterns, posture variations, minor movements, and cognitive engagement, among others. Ensuring age and sex matching of results is pivotal. While comparisons using two- or multiple-stage tests can help mitigate inter-individual differences, persistent comorbidities may continually affect individual disease conditions. Nevertheless, HRV analysis remains an effective tool for evaluating stress responses, workplace safety protocols, and ergonomic measures, as well as forecasting survival rates and disease progression across various pathologies.

However, a thorough and meticulous presentation and evaluation are essential for its application. Noteworthy features of the analysis methods include IBI preprocessing, time-domain, frequency-domain, time-frequency, and nonlinear HRV analysis. Researchers also possess the capability to fully customize the source code to align with their personal preferences or specific study requirements. These user-friendly functionalities and analysis features collectively contribute to the study of HRV.

References

[1] John T. Ramshur, "*Design, Evaluation, and Application of Heart Rate Variability Analysis Software (HRVAS)*," Electronic Theses and Dissertations, University of Memphis, pp. 1-108, 2010. [CrossRef] [Google Scholar] [Publisher Link]

[2] Fatma Sayed Ibrahim et al., "Pre-Processing Steps for Genome-Wide High-Density NARAC Dataset Facilitates its Haplotype Block Partitioning," *Journal of Advanced Engineering Trends*, vol. 40, no. 2, pp. 61-69, 2021. [CrossRef] [Google Scholar] [Publisher Link]

[3] William E. Shell Md et al., "Sentra PM (A Medical Food) and Trazodone in the Management of Sleep Disorders," *Journal of Central Nervous System Disease*, vol. 4, pp. 65-72, 2012. [CrossRef] [Google Scholar] [Publisher Link]

[4] Amira Mofreh Ibrahim, Kamel Rahouma, and Hesham Fathy Aly Hamed, "Deep Neural Network for Breast Tumor Classification through Histopathological Image," *Journal of Advanced Engineering Trends*, vol. 42, no. 1, pp. 121-129, 2022. [CrossRef] [Google Scholar] [Publisher Link]

[5] Michael Brennan, Marimuthu Palaniswami, and Peter Kamen, "Poincaré Plot Interpretation Using a Physiological Model of HRV Based on a Network of Oscillators," *American Journal of Physiology-Heart and Circulatory Physiology*, vol. 283, no. 5, pp. H1873-H1886, 2002. [CrossRef] [Google Scholar] [Publisher Link]

[6] Michael Gaebler et al., "Heart Rate Variability and its Neural Correlates during Emotional Face Processing in Social Anxiety Disorder," *Biological Psychology*, vol. 94, no. 2, pp. 319-330, 2013. [CrossRef] [Google Scholar] [Publisher Link]

[7] Teresa Henriques et al., "Nonlinear Methods Most Applied to Heart-Rate Time Series: A Review," *Entropy*, vol. 22, no. 3, pp. 1-40, 2020. [CrossRef] [Google Scholar] [Publisher Link]

[8] Antonio Cevese et al., "Baroreflex and Oscillation of Heart Period at 0.1 Hz Studied by Alpha-Blockade and Cross-Spectral Analysis in Healthy Humans," *Journal of Physiology*, vol. 531, no. 1, pp. 235-244, 2001. [CrossRef] [Google Scholar] [Publisher Link]

[9] R. Acharya et al., "Classification of Cardiac Abnormalities Using Heart Rate Signals," *Medical and Biological Engineering and Computing*, vol. 42, pp. 288-293, 2004. [CrossRef] [Google Scholar] [Publisher Link]

[10] Haitham M. Al-Angari, and Alan V. Sahakian, "Use of Sample Entropy Approach to Study Heart Rate Variability in Obstructive Sleep Apnea Syndrome," *IEEE Transactions on Biomedical Engineering*, vol. 54, no. 10, pp. 1900-1904, 2007. [CrossRef] [Google Scholar] [Publisher Link]

[11] R.E. Nabors-Oberg et al., "The Effects of Controlled Smoking on Heart Period Variability," *IEEE Engineering in Medicine and Biology Magazine*, vol. 21, no. 4, pp. 65-70, 2002. [CrossRef] [Google Scholar] [Publisher Link]

[12] D. Bonaduce et al., "Effects of Converting Enzyme Inhibition on Heart Period Variability in Patients with Acute Myocardial Infarction," *Circulation*, vol. 90, no. 1, pp. 108-113, 1994. [CrossRef] [Google Scholar] [Publisher Link]

[13] Yoko Tsui Caldwell, and Patrick R. Steffen, "Adding HRV Biofeedback to Psychotherapy Increases Heart Rate Variability and Improves the Treatment of Major Depressive Disorder," *International Journal of Psychophysiology*, vol. 131, pp. 96-101, 2018. [CrossRef] [Google Scholar] [Publisher Link]

[14] Jakub S. Gąsior et al., "Normative Values for Heart Rate Variability Parameters in School-Aged Children: Simple Approach Considering Differences in Average Heart Rate," *Frontiers in Physiology*, vol. 9, pp. 1-12, 2018. [CrossRef] [Google Scholar] [Publisher Link]

[15] Jermana Lopes de Moraes et al., "Stratification of Cardiopathies Using Photoplethysmographic Signals," *Informatics in Medicine Unlocked*, vol. 20, pp. 1-8, 2020. [CrossRef] [Google Scholar] [Publisher Link]

[16] Reena Ranpuria et al., "Heart Rate Variability (HRV) in Kidney Failure: Measurement and Consequences of Reduced HRV," *Nephrology Dialysis Transplantation*, vol. 23, no. 2, pp. 444-449, 2008. [CrossRef] [Google Scholar] [Publisher Link]

[17] Wilhelm Burger, and Mark J. Burge, *Digital Image Processing: An Algorithmic Introduction Using Java*, 2nd ed., Springer Nature, 2022. [CrossRef] [Google Scholar] [Publisher Link]

[18] Aparecida Maria Catai et al., "Heart Rate Variability: Are you Using It Properly? Standardisation Checklist of Procedures," *Brazilian Journal of Physical Therapy*, vol. 24, no. 2, pp. 91-102, 2020. [CrossRef] [Google Scholar] [Publisher Link]

[19] N. Lippman, K.M. Stein, and B.B. Lerman, "Comparison of Methods for Removal of Ectopy in Measurement of Heart Rate Variability," *American Journal of Physiology-Heart and Circulatory Physiology*, vol. 267, no. 1, pp. H411-H418, 1994. [CrossRef] [Google Scholar] [Publisher Link]

[20] Luca Faes et al., "Comparison of Methods for the Assessment of Nonlinearity in Short-Term Heart Rate Variability under Different Physiopathological States," *Chaos: An Interdisciplinary Journal of Nonlinear Science*, vol. 29, no. 12, 2019. [CrossRef] [Google Scholar] [Publisher Link]

[21] Jakob Karolus et al., "Mirror, Mirror on the Wall: Exploring Ubiquitous Artifacts for Health Tracking," *MUM '21: Proceedings of the 20th International Conference on Mobile and Ubiquitous Multimedia*, pp. 148-157, 2021. [CrossRef] [Google Scholar] [Publisher Link]

[22] K. Shafqat, S.K. Pal, and P.A. Kyriacou, "Evaluation of Two Detrending Techniques for Application in Heart Rate Variability," *2007 29th Annual International Conference of the IEEE Engineering in Medicine and Biology Society*, Lyon, France, pp. 267-270, 2007. [CrossRef] [Google Scholar] [Publisher Link]

[23] Marek Malik et al., "Heart Rate Variability: Standards of Measurement, Physiological Interpretation, and Clinical Use," *European Heart Journal*, vol. 17, no. 3, pp. 354-381, 1996. [CrossRef] [Google Scholar] [Publisher Link]

[24] Marcus Vollmer, "HRVTool - An Open-Source Matlab Toolbox for Analyzing Heart Rate Variability," *2019 Computing in Cardiology Conference (CinC)*, Singapore, pp. 1-4, 2019. [CrossRef] [Google Scholar] [Publisher Link]

[25] Dominique Makowski et al., "NeuroKit2: A Python Toolbox for Neurophysiological Signal Processing," *Behavior Research Methods*, vol. 53, pp. 1689-1696, 2021. [CrossRef] [Google Scholar] [Publisher Link]